Multibranched Gold−Mesoporous Silica Nanoparticles Coated with a Molecularly Imprinted Polymer for Label-Free Antibiotic Surface-Enhanced Raman Scattering Analysis

Sergio Carrasco,[†] Elena Benito-Peña,[†] Fernando Navarro-Villoslada,[†] Judith Langer,[‡,§,∥] Marta N. Sanz-Ortiz,[‡,§,∥] Javier Reguera,[‡,§,∥] Luis M. Liz-Marzán,[*,‡,§,∥] and María C. Moreno-Bondi[*,†]

[†]Department of Analytical Chemistry, Faculty of Chemistry, Complutense University, Ciudad Universitaria s/n, Madrid 28040, Spain

[‡]BioNanoPlasmonics Laboratory, CIC biomaGUNE, Paseo de Miramón 182, Donostia-San Sebastián 20009, Spain

[§]Biomedical Research Networking Center in Bioengineering, Biomaterials, and Nanomedicine (CIBER-BBN), Paseo Miramón 182, Donostia-San Sebastián 20009, Spain

[∥]Ikerbasque, Basque Foundation for Science, Bilbao 48013, Spain

We describe the preparation of multibranched gold−silica−molecularly imprinted polymer (bAu@mSiO$_2$@ MIP) core−shell nanoparticles, with their specific ability to recognize enrofloxacin (ENRO), and their application as label-free nanosensors for the specific detection of the antimicrobial by surface-enhanced Raman scattering. The use of these nanocomposites results in a large enhancement of the Raman scattering of ENRO upon binding of an antibiotic to the selective recognition sites in the MIP. These are in the proximity of the gold core branches that act as intrinsic hot spots providing highly localized and strongly enhanced electromagnetic fields caused by plasmon resonance. The effect of the multibranched morphology of the gold cores (bAu) on the optical spectroscopic response of the bAu@mSiO$_2$@MIP nanosensors is investigated with the aim of improving ENRO detection. The optimized nanostructures allowed us to achieve a detection limit of 1.5 nM for ENRO, which is 2 orders of magnitude lower than those for previously reported Au@MIP nanosensors, additionally providing negligible cross-reactivity toward other potential interfering species.

INTRODUCTION

Molecular imprinting allows the design and preparation of tailor-made polymer materials containing molecularly engineered receptor sites with selectivity and affinity for specific ligands that resemble those of biological systems, such as antibodies, enzymes, or other biological receptors. For polymer preparation, the selected print molecule, which can be the analyte or a surrogate molecule, interacts through covalent or noncovalent bonding. This interaction is produced with functional monomers that are polymerized in the presence of a cross-linker and the selected print molecule. The resulting three-dimensional supramolecular structure contains specific recognition sites with functional group shapes and geometries that are complementary to those present in the template molecule.[1]

Molecularly imprinted polymers (MIPs) have been widely used in different fields, such as solid phase extraction (SPE),[2] chromatography,[3] catalysis,[4] regio- and enantioselective synthesis,[5] bioremediation,[6] diagnostics,[7] and drug delivery.[8] Additionally, the use of MIPs as recognition elements in biomimetic sensing has allowed us to overcome some of the problems linked to the use of biomolecules for such applications, including production time and cost, the need for experimentation animals, long-term stability, and regeneration ability.[9,10] Moreover, these cross-linked materials are intrinsically more stable and robust than their biological counterparts, do not require cold storage and cold-chain logistics, and can be applied in harsh environments such as in the presence of organic solvents, strong acids, or bases and at high temperatures and pressures.[11] However, several drawbacks are associated with the use of MIPs for sensing applications, including the slower binding kinetics due to the usually lower affinity constants of these materials in comparison to those of biological receptors, the difficulty in transforming the binding event into a measurable signal, and the difficulties associated with multiplexed analysis.[12,13]

In an effort to circumvent some of these limitations, microfabrication processes, such as electrical deposition,[14]

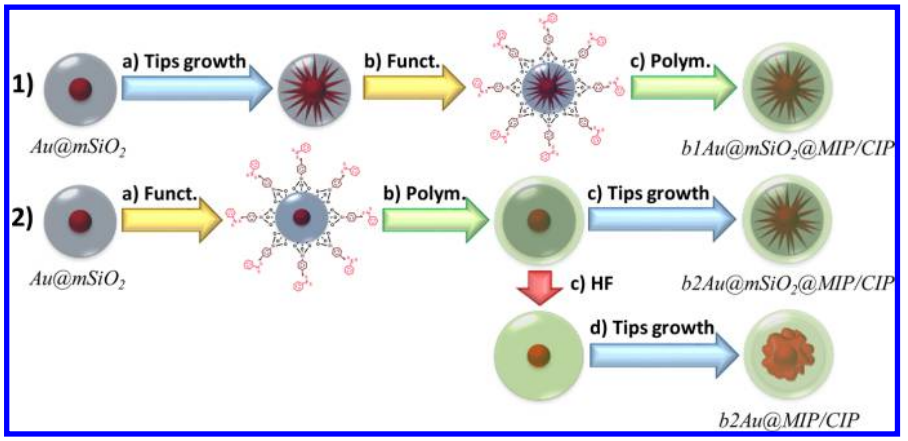

Figure 1. Schematic representation of the different nanocomposites fabricated in this work for the development of SERS nanosensors, using Au@$mSiO_2$ nanoparticles and (1) a branching–functionalization–polymerization approach to produce b1Au@$mSiO_2$@MIP/CIP (molecularly imprinted/control imprinted polymer) nanoparticles and (2) a functionalization–polymerization–branching approach to produce b2Au@$mSiO_2$@MIP/CIP or b2Au@MIP/CIP nanoparticles, including an etching step between the polymerization and branching processes for the b2 nanocomposites.

mechanical spotting,[15] optical patterning,[16] and different lithographic approaches,[17] have been described for the fabrication of MIPs.[18] Alternatively, in an effort to produce smaller nanostructures with improved sensing properties,[19] interest is now focused on the synthesis of core–shell nanocomposite MIPs that combine the selective recognition properties of the biomimetic polymer with the additional features of an inorganic core.[20] The synthesis of these nanocomposites is usually performed by controlled/living radical polymerization (CRP),[21] either by reversible addition–fragmentation chain transfer polymerization (RAFT)[22] or by atom transfer radical polymerization (ATRP).[23] These techniques allow formation of homogeneous MIP films with controlled thickness on different inorganic cores, such as magnetic nanoparticles, quantum dots, carbon nanotubes, silica nanoparticles, and metal colloids,[18] yielding well-defined core–shell structures.[24]

The use of metallic nanomaterials increases the signal-to-noise ratio in optical biosensors,[25] improving the detection limits of techniques such as, for example, colorimetry,[26] surface-enhanced Raman scattering (SERS),[27] and localized surface plasmon resonance (LSPR).[28] Among the available noble metal colloids, gold nanoparticles (AuNPs) play a key role in the development of this kind of sensor, as a direct consequence of their extraordinary electro-optical properties, biocompatibility, long-term stability, and ease of fabrication and functionalization.[29] Excitation of LSPRs strongly enhances the Raman cross section of analyte molecules located in the vicinity of the nanoparticle surface due to electromagnetic and chemical mechanisms.[30]

Fluoroquinolones are broad spectrum antimicrobials used in human and veterinary medicine to treat bacterial infections.[31] The overuse or misuse of these pharmaceuticals may give rise to the presence of their residues in animal foods, as well as to the development of bacterial resistance, which is a matter of major concern for the authorities.[32] Therefore, sensitive analytical methods are required to monitor the presence of antibiotics in foods and environmental samples.[33,34] Several MIP-based sensors for fluoroquinolone analysis have been reported in the literature.[13,35,36] Because these compounds absorb light in the UV region (λ_{exc} = 280 or 320 nm) and display relatively short Stokes shifts (~80 nm), their direct analysis is somehow limited and fluorescent MIP-based sensors using labeled derivatives and competitive assays[13] or derivatization reactions[35] have been described for the determination of ENRO in different samples.

In this article, we present a label-free SERS-based composite nanosensor that combines the selectivity of molecularly imprinted materials with the large plasmonic enhancement obtained by using multibranched gold nanoparticles (bAu) as cores. The synthesis of ENRO selective Au@MIP nanomaterials involved the growth of a nanometric mesoporous silica layer on the surface of the gold nanoparticles, the formation of branched gold inside the silica mesopores, the functionalization with a RAFT agent, which confined and promoted the creation of a selective MIP outer layer directly attached to the silica surface, and a final polymerization step in the presence of the template. The suitability of these nanocomposites for the development of MIP-based SERS nanosensors is discussed in terms of the location and integrity of the antimicrobially selective binding sites, generated following different synthetic approaches, as well as their effect on the enhancement of the SERS signal upon ENRO selective recognition.

■ RESULTS AND DISCUSSION

The nanocomposites prepared during this study (Figure 1) consisted of a gold core covered with a mesoporous silica shell further functionalized with a thin MIP layer, which is selective for the antibiotic ENRO and simultaneously allowed the growth of gold branches within the empty-channel structure. The optimal configuration of the bAu@$mSiO_2$@MIP hybrid nanoparticles (in terms of SERS performance) was selected by focusing on an effective plasmonic coupling between the gold core and ENRO molecules located inside the specific binding cavities on the MIP. Control experiments required the preparation of imprinted polymer (CIP) nanocomposites obtained under the same conditions that were used for the MIP, but in the presence of Boc-L-phenylalanine (Boc-Phe-OH), instead of ENRO, as a template molecule.

Although the specific enhancement mechanism behind SERS is far from the scope of this work,[37,38] it should be noted here that it requires the proximity of the metal core and the molecule inside the binding cavities.[39,40] For this reason, we expected that the use of mesoporous silica scaffolds would favor

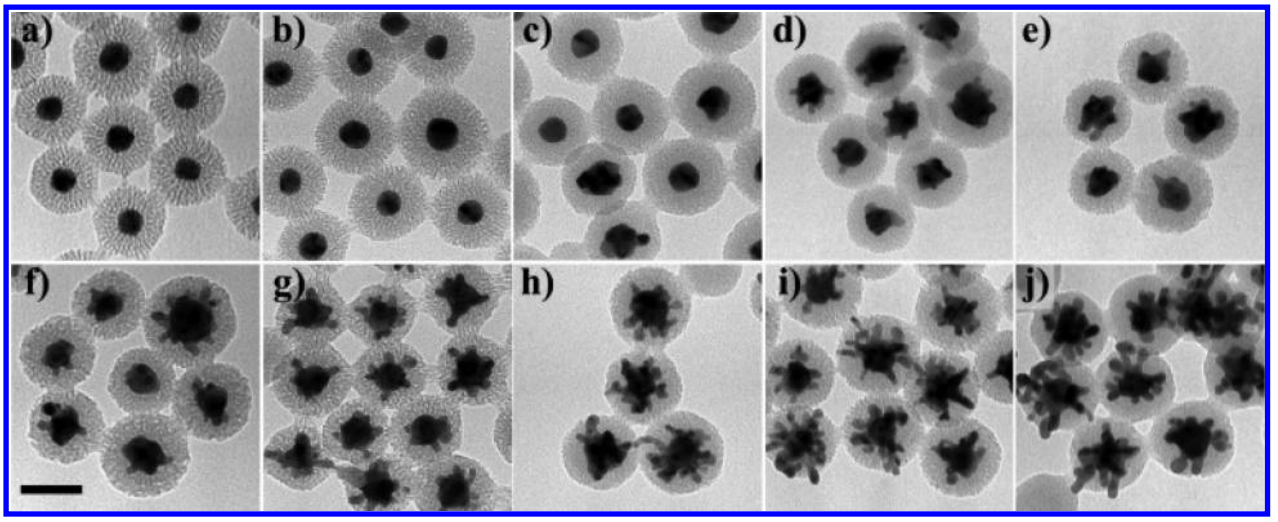

Figure 2. Transmission electron microscopy micrographs of b1Au@mSiO$_2$ nanoparticles obtained through step-by-step branching of 0.5 mM Au@mSiO$_2$ used as a seed and [Au^{3+}]/[Au^0] ratios of (a) 0.6, (b) 1.1, (c) 1.7, (d) 2.3, (e) 2.8, (f) 3.4, (g) 4.0, (h) 4.6, (i) 5.2, and (j) 5.7. The scale bar (for all images) is 50 nm.

the formation of imprinted cavities within the silica pores, close to the gold core. All our attempts to create MIP layers directly attached to the gold particles failed, as the polymerization conditions resulted in serious damage to the cores, promoting their disaggregation in the presence of radical species.[41] Therefore, silica layers accomplished three different roles: acting as a protective layer for the gold cores, acting as templates for branching of the metal cores, and acting as a substrate for the anchoring of MIP layers, after the immobilization of the RAFT agent.

Fabrication of Branched bAu@mSiO$_2$@MIP/CIP Nanoparticles. All the steps for nanostructure preparation are schematically shown in Figure 1. The process chosen for silica synthesis (details can be found in the Supporting Information) is characterized by the formation of radial channels in the silica shell connecting the gold core with the outer surface of the shell, thereby conferring an empty-channel morphology to the structure that allows, in a further step, catalytic branching from the gold core within the silica channels.[42] This approach has been exploited from different points of view, resulting in three types of branched polymer nanocomposites using Au@mSiO$_2$, which we termed b1Au@mSiO$_2$@MIP/CIP, b2Au@mSiO$_2$@MIP/CIP, and b2Au@MIP/CIP. From the nanostructures tested, only b1Au@mSiO$_2$@MIP showed both the ability to recognize ENRO and SERS activity, as will be further discussed below. See the Supporting Information for the detailed experimental procedure.

We approached the fabrication of core−shell nanocomposites by growing gold branches through the mesopores of the silica layer around gold nanospheres. Sanz-Ortiz et al. recently reported an efficient synthesis of such gold nanocomposites in a single-step branching process.[42] In the work presented here, we modified the synthetic procedure to obtain thinner mesoporous silica shells and carefully controlled the branching process.

Silica layers with radial mesoporous channels (r_{SiO_2} = 25 ± 4 nm) were formed in the presence of CTAB (Figure S1a) on citrate−gold nanospheres (r_{Au} = 7.0 ± 0.4 nm), resulting in Au@mSiO$_2$ nanocomposites. CTAB removal was required prior to branching from the gold cores. Previous studies reported a high stability of silica nanoparticles or nanolayers prepared by a modified Stöber procedure, when thermal annealing was performed after synthesis.[43−45] In this work, a 300 °C treatment for 6 h was applied prior to the functionalization−branching processes to the Au@mSiO$_2$ nanoparticles to prevent the dissolution of the silica shell in the aqueous medium.

After thermal annealing, two different approaches were followed, according to the scheme depicted in Figure 1. (1) In the first protocol, mesoporous Au@mSiO$_2$ nanocomposite particles were used as seeds to grow branches via autocatalytic reduction of HAuCl$_4$ on the spherical gold cores, yielding b1Au@mSiO$_2$ nanoparticles. The resulting branched nanoparticles were then functionalized with the RAFT agent and polymerized according to the conditions described in the Supporting Information, yielding b1Au@mSiO$_2$@MIP/CIP nanocomposites. (2) Via a second approach, Au@mSiO$_2$ nanoparticles were functionalized and polymerized prior to the branching process, yielding b2Au@mSiO$_2$@MIP/CIP nanocomposites, or b2Au@MIP/CIP if the silica was etched previously. For both approaches 1 and 2, we compared the morphology of the nanocomposites when branching was achieved in a single step or via multistep (step-by-step) growth.

Preparation of b1Au@mSiO$_2$@MIP/CIP Nanoparticles. We first evaluated direct branching versus the step-by-step growth. When 0.25 and 0.5 mM core−shell seeds were employed ([Au^{3+}]/[Au^0] = 5.7), aggregation of the nanocomposites was observed. Branched stable structures started to appear for larger amounts of seeds ([Au^0] ≥ 0.75 mM). As the concentration of seeds was increased from 0.75 to 2 mM (Figure S2), shorter branches were obtained, because the same amount of growth precursor was employed to fill a larger amount of mesoporous channels. Interestingly, better-defined branches were observed upon addition of the growth solution in several steps (step-by-step), leading to more extended branching with an increasing [Au^{3+}]/[Au^0] ratio (Figure 2).

After the last branching step, b1Au@mSiO$_2$ nanoparticles were functionalized with the RAFT agent and polymerized according to the conditions described in the Experimental Section in the Supporting Information, resulting in b1Au@mSiO$_2$@MIP/CIP hybrid polymers (Figure 3). Some nanocomposite aggregation was observed after polymerization but did not affect the stability of the solutions.

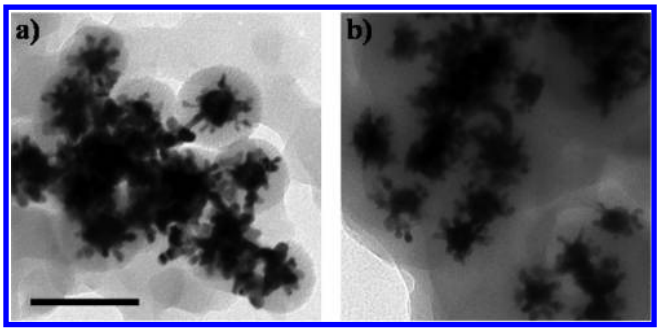

Figure 3. Transmission electron microscopy micrographs of (a) b1Au@mSiO$_2$@MIP and (b) b1Au@mSiO$_2$@CIP. The scale bar is 100 nm.

Preparation of b2Au@mSiO$_2$@MIP/CIP and b2Au@MIP/CIP Nanoparticles. In the second approach, Au@mSiO$_2$ nanoparticles were first functionalized with the RAFT agent and polymerized as in the previous case, forming Au@mSiO$_2$@MIP/CIP nanoparticles (Figure S3a,b). These nanocomposites were branched after polymerization to produce the b2Au@mSiO$_2$@MIP/CIP nanoparticles (Figure 4).

In parallel, an additional step was included between polymerization and branching, which comprised etching of the silica scaffold with HF (Figure S3c,d) to produce Au@MIP/CIP gold–polymer hybrids that were finally branched, resulting in b2Au@MIP/CIP nanocomposites (Figure S5). Branching of both types of nanoparticles, b2Au@mSiO$_2$@MIP/CIP (Figure 4) and b2Au@MIP/CIP (Figure S5), was performed following a step-by-step approach similar to that described for b1Au@mSiO$_2$@MIP/CIP. However, successful branching occurred for only b2Au@mSiO$_2$@MIP/CIP nanoparticles, leading to larger nanostar sizes with increasing [Au^{3+}]/[Au^0] ratios, while prior etching of the silica scaffold in b2Au@MIP/CIP resulted in the growth of popcornlike gold–polymer nanocomposites, as expected from the absence of the mesoporous silica channels.

Direct branching of Au@mSiO$_2$@MIP/CIP and Au@MIP/CIP was also tested, instead of the step-by-step procedure. However, in all cases, b1Au@mSiO$_2$@MIP/CIP (Figure S2), b2Au@mSiO$_2$@MIP/CIP (Figure S4a,b), and b2Au@MIP/CIP (Figure S4c,d), poorer control over branching was achieved as compared to that in the step-by step route, as the gold tips were grown from the gold core in an individual step. Nanostructures similar to those reported by Sanz-Ortiz et al. were obtained.[42] From these experiments, we conclude that the step-by-step process results in branched nanocomposites more homogeneous than those prepared in a single branching step, which allowed us to improve the distribution and quality of the gold branches compared to those achieved in earlier work.

Morphological and Spectroscopic Comparison between Branched Nanoparticles. Better-defined branched structures were obtained in b2Au@mSiO$_2$@MIP/CIP (Figure 4) than in b1Au@mSiO$_2$ (Figure 2) nanoparticles, while popcornlike gold–polymer nanocomposites were formed when the silica scaffold was previously etched [b2Au@MIP/CIP (Figure S5)]. Branching of these three nanocomposites was spectroscopically monitored, as well. Initially, for b1Au@mSiO$_2$, a bathochromic shift was observed for the plasmon band of gold nanospheres used as cores, from 522 to 537 nm, which points toward particle growth, in agreement with transmission electron microscopy (TEM) observations (Figure 5a). After the third addition, a broad band around 800 nm appeared, which shifted further to the IR after subsequent addition steps. A similar behavior was observed for b2Au@mSiO$_2$@MIP/CIP nanocomposites, but branching was observed from the first addition (Figure 5b), without an initial increase in core size. This observation is likely related to the higher degree of encapsulation of the gold core in the presence of the silica and polymer layers as compared to the previous case, where no polymer layer was present. No branches were generated in the b2Au@MIP/CIP nanocomposites, where the silica shell was etched, demonstrating the need for mesoporous channelled structures to obtain branched composites. In this case, the LSPR maximum shifted from 522 to 580 nm, indicating growth of the gold cores with a small roughness of the surface, even in the presence of the polymer, and exploiting the hollow crannies that silica left when it was removed (Figure 5c).

Development and Characterization of the SERS Nanosensor. *Evaluation of the SERS Activity of the Different Nanocomposites.* The SERS activity of ENRO was monitored by the acquisition of Raman spectra of pure antibiotic powder

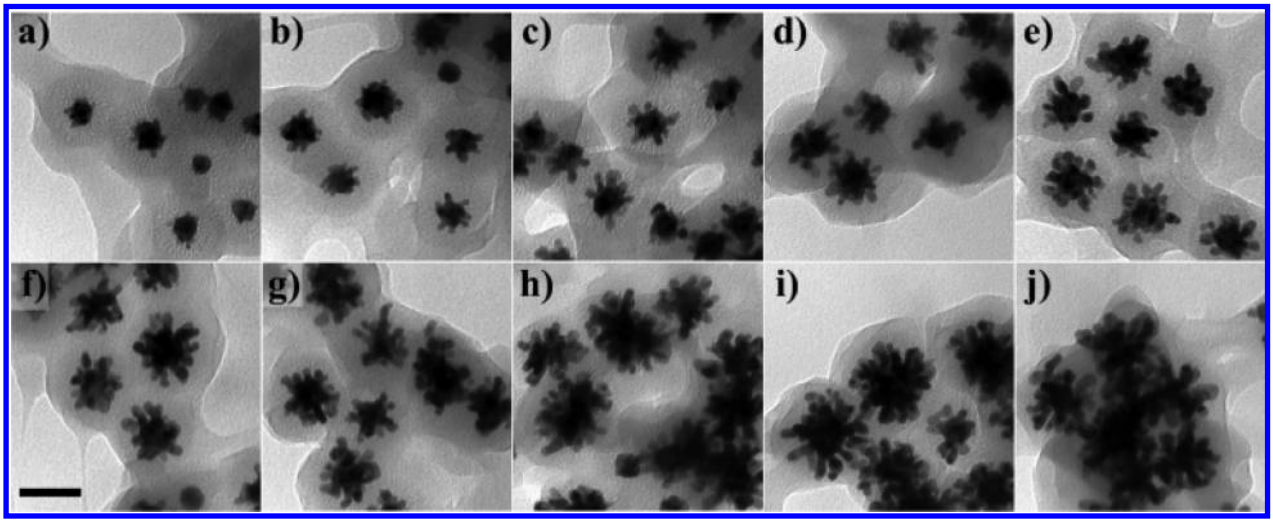

Figure 4. TEM micrographs of b2Au@mSiO$_2$@MIP nanoparticles obtained through step-by-step branching of 0.5 mM Au@mSiO$_2$@MIP used as a seed and [Au^{3+}]/[Au^0] ratios of (a) 0.6, (b) 1.1, (c) 1.7, (d) 2.3, (e) 2.9, (f) 3.5, (g) 4.2, (h) 4.8, (i) 5.5, and (j) 6.2. The scale bar is 50 nm.

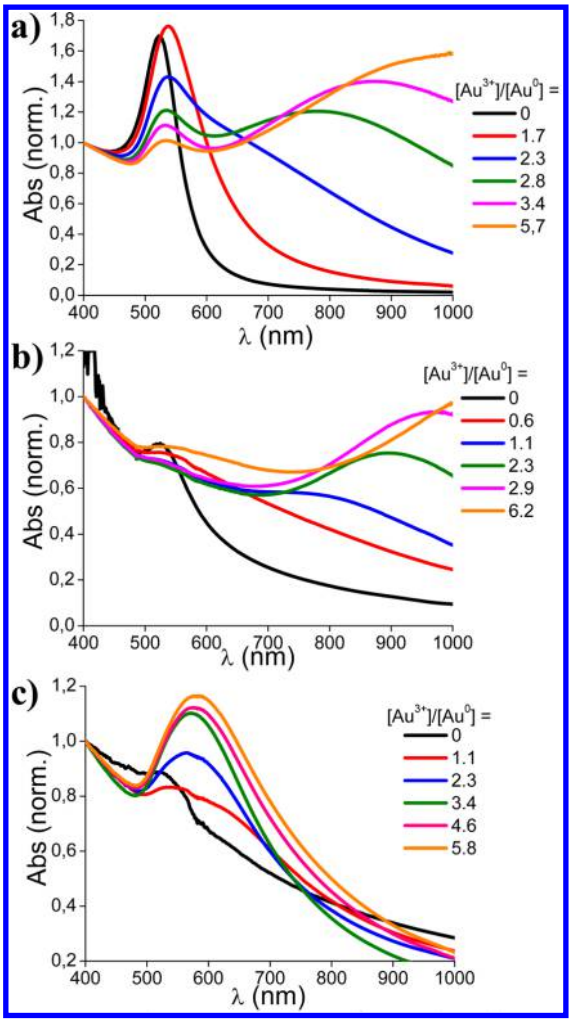

Figure 5. Absorption spectra after each addition of branching reagent: (a) b1Au@mSiO$_2$, (b) b2Au@mSiO$_2$@MIP, and (c) b2Au@MIP.

and a solution 0.1 mM ENRO in MeCN, in the presence of a 0.5 mM suspension of gold nanostars (Figure S6). The most important SERS peaks of ENRO correspond to =C−H deformation (693 cm^{-1}), methylene rocking modes (748 cm^{-1}), substituted benzene ring deformation (771 cm^{-1}), C−H rocking (1070 cm^{-1}), symmetric O−C−O stretching (1395 cm^{-1}), benzene ring vibration (1465 cm^{-1}), benzene ring stretching (1594 cm^{-1}), and C=O stretching (1624 cm^{-1}).[46,47] The peak at 1395 cm^{-1} has been previously used with satisfactory results in Raman−SERS quantification of ENRO.[48] No Raman spectra were observed for 0.1 mM ENRO in the absence of gold nanostars.

The recognition capabilities of all polymer nanocomposites fabricated in this work were evaluated through SERS experiments, at the nanoparticle and antibiotic concentrations mentioned in the Experimental Section in the Supporting Information, but only b1Au@mSiO$_2$@MIP/CIP showed SERS activity. Among all spiky structures, those in which branching was performed after polymerization, i.e., b2Au@mSiO$_2$@MIP/CIP and b2Au@MIP/CIP, did not show a detectable SERS signal. We hypothesize that the postformation of gold branches could damage the ENRO specific binding cavities during their growth, because compositions and concentrations similar to those in b1Au@mSiO$_2$@MIP/CIP nanoparticles were used. It has been reported that binding sites can occasionally collapse, even during the removal of the template molecule after polymer synthesis.[49] We speculate that tip growth takes place not only within the silica mesoporous channels but also within the imprinted pockets that ENRO creates when polymerization is induced prior to branching. On the other hand, b2Au@MIP/CIP hybrid polymers showed poor plasmon enhancement as no branched structures were obtained (see Figure S5 and Figure 5c). In the case of branched nanocomposites obtained in a single branching step, although sharpened spikes should produce larger Raman enhancements, the number of spikes was considerably lower than the number produced in the step-by-step approach. This aspect, together with the damage to the binding sites as mentioned above, resulted in negligible Raman signals.[37]

We conclude that the broad plasmon band associated with the gold branches in b1Au@mSiO$_2$@MIP/CIP produced the effective plasmon enhancement in SERS. The detection required, however, that the branching occurred before polymerization, with no chance of destroying binding cavities at locations that overlapped with the hot spots created within

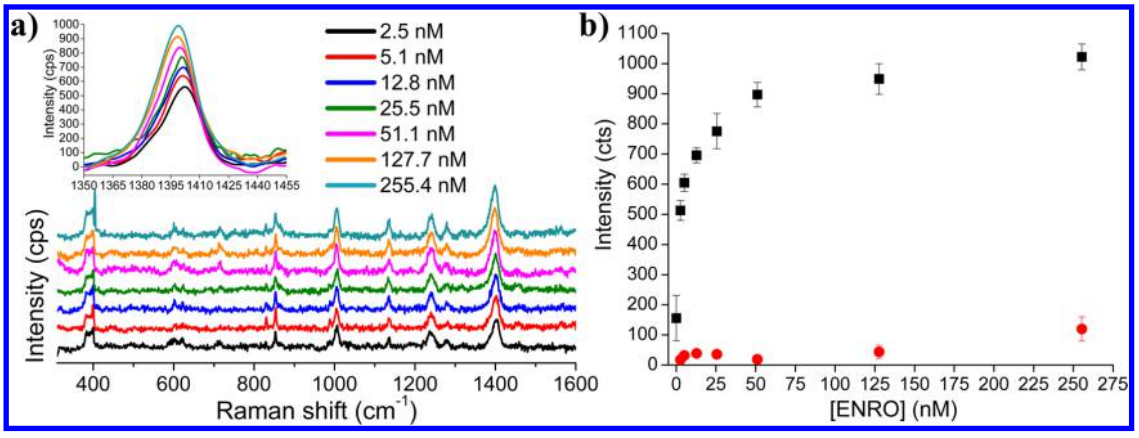

Figure 6. (a) SERS spectra of b1Au@mSiO$_2$@MIP nanoparticles incubated for 10 min in the presence of 50:50 (v/v) MeCN/HEPES (25 mM, pH 7.5) samples containing increasing concentrations of ENRO, after background correction. The inset is a close-up of the 1350−1455 cm^{-1} region, corresponding to the symmetric O−C−O stretching peak. (b) Calibration plot of b1Au@mSiO$_2$@MIP (black squares; n = 3) and b1Au@mSiO$_2$@CIP (red circles; n = 3) nanocomposites incubated with ENRO. Signals plotted correspond to the symmetric stretching of O−C−O groups at 1400 cm^{-1}.

the gold branches.[50] With regard to the incubation and measurement conditions (Table S1), we chose 25 nM nanoparticles, in terms of initial Au^0 seed concentration, to characterize the SERS substrate, as higher nanocomposite concentrations led to huge scattering effects that masked Raman signals. Moreover, no differences in the intensity of Raman peaks (<1%) were observed when incubations were performed for 10 min or 1 h (data not shown), and thus, the shorter incubation time was selected for nanosensor development.

Selectivity of the SERS b1Au@mSiO$_2$@MIP Nanosensor. The recognition capability of the SERS nanosensor based on b1Au@mSiO$_2$@MIP/CIP nanocomposites was evaluated by incubation with different ENRO concentrations (ranging from 0 to 255 nM) in 50:50 (v/v) MeCN/HEPES (25 mM, pH 7.5) media (Table S2). This incubation medium was selected according to our previous results using the same MIP composition for ENRO analysis.[13]

After background correction of the SERS spectra (Figure 6a), the intensities of the peak centered at ∼1400 cm^{-1} were plotted versus ENRO concentration, yielding the corresponding calibration curves (Figure 6b). A residual peak (intensity of 156 ± 75 cps) at the same wavenumber was observed for MIP nanocomposites, in the absence of the template molecule (first black point of the calibration curve in Figure 6b), demonstrating that methacrylic acid (MAA) units (with a similar O−C−O stretching to ENRO),[51] and thus the specific recognition cavities, were incorporated in the proximity of the gold branches. In CIP nanocomposites, on the other hand, a negligible signal was observed for this wavenumber value, showing that complementary cavities are located farther from the Au tips than in MIP, as previously discussed, together with the different reactivity of the prepolymerization mixture in the presence of different templates.[52−54] Furthermore, a small red-shift, from 1407 to 1398 cm^{-1}, was observed for the Raman peaks used for quantification as the ENRO concentration was increased (inset of Figure 6a). This is in agreement with the hypothesis regarding the location of binding sites, as the former Raman shift is more similar to that of individual MAA units and the latter can be assigned to ENRO.

No measurable recognition of ENRO by b1Au@mSiO$_2$@CIP nanoparticles was observed, demonstrating the efficient molecular imprinting process. Fitting calibration data of b1Au@mSiO$_2$@MIP, on the logarithmic *x*-axis, with a linear regression model [r^2 = 0.991 (Figure S7)] results in a LOD and a limit of quantification (LOQ) of 1.5 and 3.7 nM, respectively, calculated as ks_o/b, where *k* equals 3 (LOD) or 10 (LOQ), s_o is the standard deviation of the intercept, and *b* is the slope.[55] The obtained LOD for the SERS substrate yields one of the lowest values reported in the literature for this antibiotic detection and is 2 orders of magnitude lower than those of other Au@MIP SERS-based nanosensors.[56]

Cross-Reactivity of the SERS Nanosensor. Recognition of b1Au@mSiO$_2$@MIP/CIP nanocomposites toward potential interfering species was also evaluated. Ampicillin (AMPI), penicillin G streptomycin (PENGS), and templates used for the synthesis of MIP and CIP nanoparticles, i.e., ENRO and Boc-Phe-OH, were tested at the highest concentration (250 nM) assayed to produce the calibration plots (Table S3). The chemical structures of interfering molecules used for this study can be seen in Figure S8. These molecules bear a carboxylic acid group with symmetric O−C−O stretching vibrations leading to a Raman peak at ∼1400 cm^{-1}, which was used for quantification of each analyte bound to the MIP/CIP nanocomposites.[46−48,57−60] The results are summarized in Table 1.

Table 1. Intensities of Raman Peaks at 1400 cm^{-1} Corresponding to the Symmetric O−C−O Stretching of the Carboxylic Acid−Carboxylate Moiety of the Analytes Used for the Cross-Reactivity Study[a]

analyte	b1Au@mSiO$_2$@MIP (cps)	b1Au@mSiO$_2$@CIP (cps)
PENGS	103 ± 63	153 ± 72
AMPI	209 ± 44	168 ± 51
Boc-Phe-OH	NM[b]	455 ± 35
ENRO	1022 ± 43	120 ± 40

[a]Incubation (n = 3) was performed in the presence of 250 nM interfering species for 10 min. [b]No discernible Raman signal was recorded.

Selective recognition of ENRO was observed in only b1Au@mSiO$_2$@MIP, as the polymer precursor included this antibiotic during polymerization. It is also reasonable to determine the recognition ability of b1Au@mSiO$_2$@CIP nanoparticles toward Boc-Phe-OH, because this was the template molecule used during their synthesis, thereby demonstrating the power of molecular imprinting polymers with these highly efficient nanocomposites. Significantly weaker SERS signals were obtained when MIP and CIP were incubated in the presence of Boc-Phe-OH and ENRO, respectively. The intensity of the ENRO signal corresponds to 26% of that of Boc-Phe-OH in the CIP, while the signal for Boc-Phe-OH in the MIP was negligible. Neither PENGS nor AMPI was selectively recognized by both nanocomposites, being 10 and 20% of the ENRO signal in MIP and 34 and 37% of the Boc-Phe-OH signal in CIP, respectively.

CONCLUSIONS

We described a new SERS nanosensor based on gold−silica−polymer nanocomposites for the selective recognition of ENRO. Exhaustive efforts focused on the synthetic procedures for obtaining efficient Raman enhancement. Thick mesoporous silica shells covering gold nanospheres, with the ability to direct the growth of gold branches from the gold core, were selected for the sensing experiments. We found that nanoparticle branching must be conducted in successive discrete steps, prior to polymerization, as wreckage of the binding sites was observed when it was performed after fabrication of the polymer layer. The methacrylic-based polymer shell of the optimized gold nanocomposites showed the binding sites located within and on the mesoporous silica structure, promoting SERS activity when ENRO was selectively recognized by the MIP, as their spatial arrangement overlaps with the hot spots created by the gold branches. Therefore, the SERS nanosensor presented in this work showed a double selectivity, one coming from the imprinting technology, as a control imprinted polymer was not able to selectively recognize ENRO, and the other stemming from the analytical technique, as the enhanced Raman spectra were different for each analyte. The analytical performance yielded a LOD of 1.5 nM for the optimized assay after incubation for only 10 min, with a limited cross-reactivity toward potential interfering species. This results in a detailed and systematic approach that yielded the lowest LOD for SERS nanosensors based on Au@MIP nanoparticles reported in the literature so far.

■ ASSOCIATED CONTENT

Supporting Information

The Supporting Information is available free of charge on the ACS Publications website at DOI: 10.1021/acs.chemmater.6b03613.

Experimental section and figures depicting data for the nanocomposites based on gold-branched nanostructures, SERS activity, selectivity, and cross-reactivity of the developed nanosensor (PDF)

■ AUTHOR INFORMATION

Corresponding Authors

*E-mail: llizmarzan@cicbiomagune.es.

*E-mail: mcmbondi@ucm.es. Phone: 0034-91394-5147. Fax: 0034-91394-4329.

Notes

The authors declare no competing financial interest.

■ ACKNOWLEDGMENTS

S.C. thanks the Ministry of Education, Culture and Sport for a doctoral grant (FPU). Financial support from MINECO (CTQ2015-69278-C2-1R) and the European Union Seventh Framework Programme (FP7/2007-2013 under Grant Agreement 312184, SACS). L.M.L.-M. acknowledges funding from the European Research Council (ERC Advanced Grant Plasmaquo).

■ REFERENCES

(1) Haupt, K. *Molecular Imprinting*; Springer-Verlag: Berlin, 2012; Vol. *325*, p 362.

(2) Turiel, E.; Martín-Esteban, A. Molecularly imprinted polymers for solid-phase microextraction. *J. Sep. Sci.* **2009**, *32*, 3278−3284.

(3) Barahona, F.; Turiel, E.; Cormack, P. A. G.; Martín-Esteban, A. Chromatographic performance of molecularly imprinted polymers: Core-shell microspheres by precipitation polymerization and grafted MIP films via iniferter-modified silica beads. *J. Polym. Sci., Part A: Polym. Chem.* **2010**, *48*, 1058−1066.

(4) Wulff, G. Models of The Binding Sites of Enzymes: Template Induced Preparation of Specific Binding Sites in Crosslinked Polymers. In *Advances in Molecular and Cell Biology*; Bittar, B. D., Lelf, B., Eds.; Elsevier: Amsterdam, 1996; Vol. *15*, pp 639−649.

(5) Alexander, C.; Smith, C. R.; Whitcombe, M. J.; Vulfson, E. N. Imprinted Polymers as Protecting Groups for Regioselective Modification of Polyfunctional Substrates. *J. Am. Chem. Soc.* **1999**, *121*, 6640−6651.

(6) Bach, M.; Tovar, G. E. M.; Weber, A. Molecularly Imprinted Polymers as Traps for Environmental and Bioremediation Applications. In *Handbook of Molecularly Imprinted Polymers*; Álvarez-Lorenzo, C., Concheiro, Á., Eds.; Smithers Rapra Technology Ltd.: Shrewsbury, U.K., 2013; pp 229−258.

(7) Bedwell, T. S.; Whitcombe, M. J. Analytical applications of MIPs in diagnostic assays: future perspectives. *Anal. Bioanal. Chem.* **2016**, *408*, 1735−1751.

(8) Álvarez-Lorenzo, C.; Concheiro, Á. Molecularly Imprinted Polymers as Components of Drug Delivery Systems. In *Handbook of Molecularly Imprinted Polymers*; Álvarez-Lorenzo, C., Concheiro, Á., Eds.; Smithers Rapra Technology Ltd.: Shrewsbury, U.K., 2013; pp 309−349.

(9) Lee, S.-W.; Kunitake, T. *Handbook of Molecular Imprinting: Advanced Sensor Applications*; Pan Stanford Publishing Pte. Ltd.: Singapore, 2013; p 609.

(10) Li, J.; Wei, G.; Zhang, Y. Molecularly Imprinted Polymers as Recognition Elements in Sensors. In *Molecularly Imprinted Sensors*; Elsevier: Amsterdam, 2012; Chapter 2, pp 35−55.

(11) Moreno-Bondi, M.; Navarro-Villoslada, F.; Benito-Pena, E.; Urraca, J. Molecularly Imprinted Polymers as Selective Recognition Elements in Optical Sensing. *Curr. Anal. Chem.* **2008**, *4*, 316−340.

(12) Suriyanarayanan, S.; Cywinski, P. J.; Moro, A. J.; Mohr, G. J.; Kutner, W. Chemosensors Based on Molecularly Imprinted Polymers. In *Molecular Imprinting*; Haupt, K., Ed.; Springer: Berlin, 2012; pp 165−265.

(13) Carrasco, S.; Benito-Pena, E.; Walt, D. R.; Moreno-Bondi, M. C. Fiber-optic array using molecularly imprinted microspheres for antibiotic analysis. *Chem. Sci.* **2015**, *6*, 3139−3147.

(14) Reculusa, S.; Heim, M.; Gao, F.; Mano, N.; Ravaine, S.; Kuhn, A. Design of Catalytically Active Cylindrical and Macroporous Gold Microelectrodes. *Adv. Funct. Mater.* **2011**, *21*, 691−698.

(15) Sokuler, M.; Gheber, L. A. Nano Fountain Pen Manufacture of Polymer Lenses for Nano-biochip Applications. *Nano Lett.* **2006**, *6*, 848−853.

(16) Conrad, P. G.; Nishimura, P. T.; Aherne, D.; Schwartz, B. J.; Wu, D.; Fang, N.; Zhang, X.; Roberts, M. J.; Shea, K. J. Functional Molecularly Imprinted Polymer Microstructures Fabricated Using Microstereolithography. *Adv. Mater.* **2003**, *15*, 1541−1544.

(17) Carrasco, S.; Canalejas-Tejero, V.; Navarro-Villoslada, F.; Barrios, C. A.; Moreno-Bondi, M. C. Cross-linkable linear copolymer with double functionality: resist for electron beam nanolithography and molecular imprinting. *J. Mater. Chem. C* **2014**, *2*, 1400−1403.

(18) Bompart, M.; Haupt, K.; Ayela, C. Micro and Nanofabrication of Molecularly Imprinted Polymers. In *Molecular Imprinting*; Haupt, K., Ed.; Springer: Berlin, 2012; pp 83−110.

(19) Vautrin-Ul, C. Overview of the Field. In *Nanosciences and Nanotechnology: Evolution or Revolution?*; Lourtioz, J.-M., Lahmani, M., Dupas-Haeberlin, C., Hesto, P., Eds.; Springer International Publishing: Cham, Switzerland, 2016; pp 113−174.

(20) Ye, L. Synthetic Strategies in Molecular Imprinting. In *Molecularly Imprinted Polymers in Biotechnology*; Mattiasson, B., Ye, L., Eds.; Springer International Publishing: Cham, Switzerland, 2015; Vol. *150*, pp 1−34.

(21) Matyjaszewski, K. Radical Polymerization. In *Controlled and Living Polymerizations*; Müller, A. H. E., Matyjaszewski, K., Eds.; Wiley-VCH Verlag GmbH & Co. KGaA: Weinheim, Germany, 2010; pp 103−166.

(22) Asman, S.; Mohamad, S.; Sarih, N. Effects of RAFT Agent on the Selective Approach of Molecularly Imprinted Polymers. *Polymers* **2015**, *7*, 484−503.

(23) Adali-Kaya, Z.; Tse Sum Bui, B.; Falcimaigne-Cordin, A.; Haupt, K. Molecularly Imprinted Polymer Nanomaterials and Nanocomposites: Atom-Transfer Radical Polymerization with Acidic Monomers. *Angew. Chem., Int. Ed.* **2015**, *54*, 5192−5195.

(24) Carter, S. R.; Rimmer, S. Surface Molecularly Imprinted Polymer Core−Shell Particles. *Adv. Funct. Mater.* **2004**, *14*, 553−561.

(25) Holzinger, M.; Le Goff, A.; Cosnier, S. Nanomaterials for biosensing applications: A Review. *Front. Chem.* **2014**, *2*, 63.

(26) Thanh, N. T. K.; Rosenzweig, Z. Development of an Aggregation-Based Immunoassay for Anti-Protein A Using Gold Nanoparticles. *Anal. Chem.* **2002**, *74*, 1624−1628.

(27) Guarrotxena, N.; Bazan, G. C. Antibody-functionalized SERS tags with improved sensitivity. *Chem. Commun.* **2011**, *47*, 8784−8786.

(28) Szunerits, S.; Boukherroub, R. Sensing using localised surface plasmon resonance sensors. *Chem. Commun.* **2012**, *48*, 8999−9010.

(29) Valcárcel, M.; López-Lorente, Á. L. Gold Nanoparticles in Analytical Chemistry. In *Comprehensive Analytical Chemistry*; Barceló, D., Ed.; Elsevier: Amsterdam, 2014; Vol. *66*, pp 3−622.

(30) Volkert, A. A.; Haes, A. J. Advancements in nanosensors using plastic antibodies. *Analyst* **2014**, *139*, 21−31.

(31) Sheehan, G.; Chew, N. S. Y. The history of quinolones. In *Fluoroquinolone Antibiotics*; Ronald, A. R., Low, D. E., Eds.; Birkhäuser: Basel, Switzerland, 2003; pp 1−10.

(32) Amábile-Cuevas, C. F. Global Perspectives of Antibiotic Resistance. In *Antimicrobial Resistance in Developing Countries*; Sosa, d. J. A., Byarugaba, K. D., Amábile-Cuevas, F. C., Hsueh, P.-R., Kariuki, S., Okeke, N. I., Eds.; Springer: New York, 2010; pp 3−13.

(33) Petrovic, M.; Radjenovic, J.; Postigo, C.; Kuster, M.; Farre, M.; Alda, M. D.; Barceló, D. Emerging Contaminants in Waste Waters: Sources and Occurrence. In *Emerging Contaminants from Industrial and Municipal Waste*; Barceló, D., Petrovic, M., Eds.; Springer: Berlin, 2008; pp 1−35.
(34) (a) Water Framework Directive 2000/60/EC; European Union: Brussels, 2000. (b) Directive 2008/105/EC; European Union: Brussels, 2008.
(35) Zdunek, J.; Benito-Peña, E.; Linares, A.; Falcimaigne-Cordin, A.; Orellana, G.; Haupt, K.; Moreno-Bondi, M. C. Surface-Imprinted Nanofilaments for Europium-Amplified Luminescent Detection of Fluoroquinolone Antibiotics. *Chem. - Eur. J.* **2013**, *19*, 10209−10216.
(36) Ton, X.-A.; Acha, V.; Haupt, K.; Tse Sum Bui, B. Direct fluorimetric sensing of UV-excited analytes in biological and environmental samples using molecularly imprinted polymer nanoparticles and fluorescence polarization. *Biosens. Bioelectron.* **2012**, *36*, 22−28.
(37) Hutter, E.; Fendler, J. H. Exploitation of Localized Surface Plasmon Resonance. *Adv. Mater.* **2004**, *16*, 1685−1706.
(38) Schatz, G. C.; Young, M. A.; Duyne, R. P. Electromagnetic Mechanism of SERS. In *Surface-Enhanced Raman Scattering: Physics and Applications*; Kneipp, K., Moskovits, M., Kneipp, H., Eds.; Springer: Berlin, 2006; pp 19−45.
(39) Pieczonka, N. W.; Goulet, P. G.; Aroca, R. Applications of the Enhancement of Resonance Raman Scattering and Fluorescence by Strongly Coupled Metallic Nanostructures. In *Surface-Enhanced Raman Scattering*; Kneipp, K., Moskovits, M., Kneipp, H., Eds.; Springer: Berlin, 2006; Vol. *103*, pp 197−216.
(40) Jensen, L.; Aikens, C. M.; Schatz, G. C. Electronic structure methods for studying surface-enhanced Raman scattering. *Chem. Soc. Rev.* **2008**, *37*, 1061−1073.
(41) Zhang, Z.; Berg, A.; Levanon, H.; Fessenden, R. W.; Meisel, D. On the Interactions of Free Radicals with Gold Nanoparticles. *J. Am. Chem. Soc.* **2003**, *125*, 7959−7963.
(42) Sanz-Ortiz, M. N.; Sentosun, K.; Bals, S.; Liz-Marzán, L. M. Templated Growth of Surface Enhanced Raman Scattering-Active Branched Gold Nanoparticles within Radial Mesoporous Silica Shells. *ACS Nano* **2015**, *9*, 10489−10497.
(43) Kobayashi, M.; Skarba, M.; Galletto, P.; Cakara, D.; Borkovec, M. Effects of heat treatment on the aggregation and charging of Stöber-type silica. *J. Colloid Interface Sci.* **2005**, *292*, 139−147.
(44) Choi, J.; Han, Y.; Park, S.; Park, J.; Kim, H. Pore Characteristics and Hydrothermal Stability of Mesoporous Silica: Role of Oleic Acid. *J. Nanomater.* **2014**, *2014*, 580347.
(45) Wong, Y. J.; Zhu, L.; Teo, W. S.; Tan, Y. W.; Yang, Y.; Wang, C.; Chen, H. Revisiting the Stöber Method: Inhomogeneity in Silica Shells. *J. Am. Chem. Soc.* **2011**, *133*, 11422−11425.
(46) Zhang, Y.; Huang, Y.; Zhai, F.; Du, R.; Liu, Y.; Lai, K. Analyses of enrofloxacin, furazolidone and malachite green in fish products with surface-enhanced Raman spectroscopy. *Food Chem.* **2012**, *135*, 845−850.
(47) Xu, Y.; Du, Y.; Li, Q.; Wang, X.; Pan, Y.; Zhang, H.; Wu, T.; Hu, H. Ultrasensitive Detection of Enrofloxacin in Chicken Muscles by Surface-Enhanced Raman Spectroscopy Using Amino-Modified Glycidyl Methacrylate-Ethylene Dimethacrylate (GMA-EDMA) Powdered Porous Material. *Food Anal. Method.* **2014**, *7*, 1219−1228.
(48) He, L.; Lin, M.; Li, H.; Kim, N.-J. Surface-enhanced Raman spectroscopy coupled with dendritic silver nanosubstrate for detection of restricted antibiotics. *J. Raman Spectrosc.* **2010**, *41*, 739−744.
(49) Lorenzo, R.; Carro, A.; Alvarez-Lorenzo, C.; Concheiro, A. To Remove or Not to Remove? The Challenge of Extracting the Template to Make the Cavities Available in Molecularly Imprinted Polymers (MIPs). *Int. J. Mol. Sci.* **2011**, *12*, 4327−4347.
(50) Brus, L. Noble Metal Nanocrystals: Plasmon Electron Transfer Photochemistry and Single-Molecule Raman Spectroscopy. *Acc. Chem. Res.* **2008**, *41*, 1742−1749.
(51) Lando, J. B.; Koenig, J. L.; Semen, J. Conformational studies of poly(methacrylic Acid). II. Laser-excited Raman studies of the conformational transition in aqueous solution. *J. Macromol. Sci., Part B: Phys.* **1973**, *7*, 319−343.
(52) Benito-Peña, E.; Moreno-Bondi, M. C.; Aparicio, S.; Orellana, G.; Cederfur, J.; Kempe, M. Molecular Engineering of Fluorescent Penicillins for Molecularly Imprinted Polymer Assays. *Anal. Chem.* **2006**, *78*, 2019−2027.
(53) Venkatesh, S.; Sizemore, S. P.; Byrne, M. E. Biomimetic hydrogels for enhanced loading and extended release of ocular therapeutics. *Biomaterials* **2007**, *28*, 717−724.
(54) Cederfur, J.; Pei, Y.; Zihui, M.; Kempe, M. Synthesis and Screening of a Molecularly Imprinted Polymer Library Targeted for Penicillin G. *J. Comb. Chem.* **2003**, *5*, 67−72.
(55) Konieczka, P.; Namiesnik, J. Method Validation. In *Quality Assurance and Quality Control in the Analytical Chemical Laboratory: A Practical Approach*; CRC Press: Boca Raton, FL, 2009; pp 131−216.
(56) Ahmad, R.; Felidj, N.; Boubekeur-Lecaque, L.; Lau-Truong, S.; Gam-Derouich, S.; Decorse, P.; Lamouri, A.; Mangeney, C. Water-soluble plasmonic nanosensors with synthetic receptors for label-free detection of folic acid. *Chem. Commun.* **2015**, *51*, 9678−9681.
(57) Wang, P.; Pang, S.; Zhang, H.; Fan, M.; He, L. Characterization of Lactococcus lactis response to ampicillin and ciprofloxacin using surface-enhanced Raman spectroscopy. *Anal. Bioanal. Chem.* **2016**, *408*, 933−941.
(58) Andreou, C.; Mirsafavi, R.; Moskovits, M.; Meinhart, C. D. Detection of low concentrations of ampicillin in milk. *Analyst* **2015**, *140*, 5003−5005.
(59) Jeffers, R. B.; Cooper, J. B. FT-Surface-Enhanced Raman Scattering of Phenylalanine Using Silver-Coated Glass Fiber Filters. *Spectrosc. Lett.* **2010**, *43*, 220−225.
(60) Clarke, S. J.; Littleford, R. E.; Smith, W. E.; Goodacre, R. Rapid monitoring of antibiotics using Raman and surface enhanced Raman spectroscopy. *Analyst* **2005**, *130*, 1019−1026.

DOI: 10.1021/acs.chemmater.6b03613
Chem. Mater. 2016, 28, 7947−7954